

Discrete-Time Dynamic-Decoupled Current Control for LCL-Equipped High-Speed Permanent Magnet Synchronous Machines

Yao, Yu; Huang, Yunkai; Peng, Fei; Dong, Jianning; Zhu, Zichong

DOI

[10.1109/TIE.2021.3127051](https://doi.org/10.1109/TIE.2021.3127051)

Publication date

2022

Document Version

Final published version

Published in

IEEE Transactions on Industrial Electronics

Citation (APA)

Yao, Y., Huang, Y., Peng, F., Dong, J., & Zhu, Z. (2022). Discrete-Time Dynamic-Decoupled Current Control for LCL-Equipped High-Speed Permanent Magnet Synchronous Machines. *IEEE Transactions on Industrial Electronics*, 69(12), 12414-12425. <https://doi.org/10.1109/TIE.2021.3127051>

Important note

To cite this publication, please use the final published version (if applicable). Please check the document version above.

Copyright

Other than for strictly personal use, it is not permitted to download, forward or distribute the text or part of it, without the consent of the author(s) and/or copyright holder(s), unless the work is under an open content license such as Creative Commons.

Takedown policy

Please contact us and provide details if you believe this document breaches copyrights. We will remove access to the work immediately and investigate your claim.

Green Open Access added to TU Delft Institutional Repository

'You share, we take care!' - Taverne project

<https://www.openaccess.nl/en/you-share-we-take-care>

Otherwise as indicated in the copyright section: the publisher is the copyright holder of this work and the author uses the Dutch legislation to make this work public.

Discrete-Time Dynamic-Decoupled Current Control for *LCL*-Equipped High-Speed Permanent Magnet Synchronous Machines

Yu Yao , Student Member, IEEE, Yunkai Huang , Fei Peng , Member, IEEE, Jianning Dong , Member, IEEE, and Zichong Zhu , Student Member, IEEE

Abstract—This article proposes a discrete-time dynamic-decoupled current controller for an *LCL*-equipped high-speed permanent magnet synchronous machine with only the motor currents measured. The controller is designed in the synchronous coordinate based on a complex *z*-domain transfer function. The main contribution of the proposed current controller is the robust dynamic decoupling performance to achieve better transient behavior. Moreover, an effective coefficient selection method is developed to acquire sufficient phase margin and gain margin, even with the system parameters varying $\pm 50\%$. Additionally, the stable region of the *LCL* resonance with the proposed method is discussed. Finally, the effectiveness of the proposed method is verified by driving the tested motor to 100 kr/min.

Index Terms—Coefficient selection, current control, high-speed surface-mounted permanent magnet synchronous machine (HSPMSM), *LCL* filter, robust dynamic decoupling, stable region.

I. INTRODUCTION

HIGH-SPEED surface-mounted permanent magnet synchronous machines (HSPMSMs) are widely used in the industrial applications, including turbine air blowers, turbine compressors, microturbine generators, and pumps because of its high power density, high efficiency, and free-gearbox operation [1]. However, since the small stator inductance and the limited switching frequency of the inverter, the high current ripple occurs in the winding current, which brings additional losses on both the stator and the rotor. Inevitably, the system efficiency is reduced. To filter the output current, an output *LCL* filter is

often adopted [2]. However, the resonance caused by the *LCL* circuit is introduced in the current control loop and it results in the instability of the closed-loop system.

Significant research efforts have been established to develop active damping (AD) strategies to effectively deal with this resonance problem, which can be classified into following categories [3], [4]: inherent damping (ID) [5]–[7], filter-based method [8]–[10], virtual-resistance method [11]–[16], full-state feedback control (FSFC) method [17]–[20], and other methods [15], [21]–[23]. In the full-digital control system, the digital-time computation delay and the pulsewidth modulation delay introduce the ID into the current control loop and it will stabilize the single-loop system [7]. The selection of the feedback loop relies on the location of the resonance frequency [5]. But when the resonance frequency crosses through the critical frequency (i.e., one-sixth of the sampling frequency) resulting from the parameter variation, the ID cannot work under this case. In the unstable region of ID, the extra AD methods are necessary. Filter-based methods aim at providing a phase-lead or phase-lag effect by introducing a filter network [8]. High-pass filter [10] and the notch filter [9] are popularly used. No additional sensors are used. The virtual-resistance methods are derived from the passive damping (PD), but the real damping resistance in the PD is replaced by the virtual resistance, which is induced by the extra feedback loop. The capacitor current feedback is adopted in [11]. And in [13], the filtered capacitor voltage is feedforward into the current control loop. Clearly, the additional sensors are necessary compared with the ID and the filter-based methods. The FSFC methods [17]–[19], [24] can achieve AD and bandwidth arrangement easily with arbitrary pole placement, but it needs all the states are measured and, thus, increases system cost and complexity.

For the *LCL*-equipped HSPMSM drive, the fundamental frequency is fast changed during the speed-dynamic process. In that case, the transient performance of the current control is difficult to be guaranteed if a stationary controller (e.g., proportional resonance controller) is implemented. Therefore, the current controller established in *dq* synchronous coordinate is preferred for the HSPMSM drives. For the *dq* controller, one problem is eliminating the coupling between the *dq* coordinate to improve the transient behavior. The robust dynamic-decoupled current control methods are proposed in [25]–[28], but their experimental plant is *L*-type converter or machines, which are

Manuscript received April 19, 2021; revised June 11, 2021 and October 25, 2021; accepted October 30, 2021. Date of publication November 16, 2021; date of current version July 8, 2022. This work was supported in part by the National Natural Science Foundation of China under Grant 51777034 and Grant 51707037 and in part by the Excellence Project Funds of Southeast University. (Corresponding author: Yunkai Huang.)

Yu Yao, Yunkai Huang, and Fei Peng are with the School of Electrical Engineering, Southeast University, Nanjing 210096, China (e-mail: yuyao@seu.edu.cn; huangyk@seu.edu.cn; pengfei@seu.edu.cn).

Jianning Dong is with the Delft University of Technology, 2628 CD Delft, The Netherlands (e-mail: J.Dong-4@tudelft.nl).

Zichong Zhu is with the School of Electrical Engineering and Control Science, Nanjing Tech University, Nanjing 211816, China (e-mail: zhu_zichong@njtech.edu.cn).

Color versions of one or more figures in this article are available at <https://doi.org/10.1109/TIE.2021.3127051>.

Digital Object Identifier 10.1109/TIE.2021.3127051

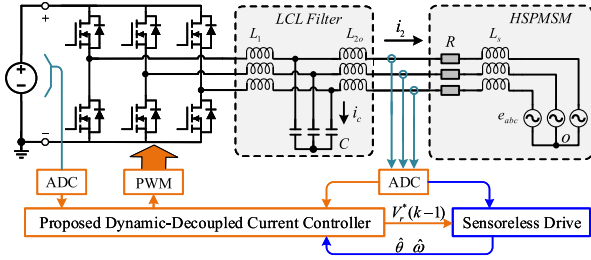


Fig. 1. System diagram of the HSPMSM drives equipped with LCL filter.

not suitable for the LCL -type applications. Wang *et al.*[29] propose a current decoupling method based on active disturbance rejection method for LCL -type STATCOM, but no experimental validations. In [30], the internal model-based current controller is implemented to achieve resonance damping and the dynamic decoupling. But when the mismatched parameters are adopted, it is difficult to ensure the decoupling capability on the premise of the required control bandwidth. Additionally, it should be noted that both methods are designed for the grid-connected converter and developed in the continuous-time domain. For the HSPMSM drive, there are the following two challenges: 1) The high fundamental frequency enhances the coupling between the dq coordinate. 2) The current controller should be developed in the discrete-time domain to achieve better overall stability under the low ratio of sampling-to-fundamental frequency.

To solve the aforementioned problems, this article proposes a novel discrete-time dynamic-decoupled current controller for LCL -equipped HSPMSM drives. The controller is designed in the dq synchronous coordinate. Compared with conventional methods, the proposed current control method has the following advantages.

- 1) Robust dynamic decoupling capability to achieve better transient performance.
- 2) Robust coefficient selection method to achieve sufficient phase margin (PM) and gain margin (GM), even with the system parameters varying $\pm 50\%$.

Finally, the effectiveness of the proposed method is verified by driving the tested HSPMSM up to 100 kr/min (1667 Hz).

II. SYSTEM DESCRIPTION AND DISCRETE-TIME MODEL

Fig. 1 shows the diagram of the HSPMSM drives equipped with LCL filter. The motor current and the dc voltage are measured. For the high-speed applications, the rotor position sensor is often not welcome or not possible because of the cost requirement, limited space, and reliability consideration. Therefore, position sensorless drive is preferred in HSPMSM drives. The position sensorless drive is based on the back electromotive force (EMF) estimation by a linear state observer [17], [31] and a phased-locked loop. Considering that this article focuses on the dynamic-decoupled current controller design, the details on the position estimation method will not be discussed.

A. Discrete-Time Model

Because of the winding resistance is usually small, it can be neglected when modeling the drive system. In that case, the complex continuous-time model in the $\alpha\beta$ stationary coordinate is derived as

$$G_s(s) = \frac{i_{2s}(s)}{V_s(s)} = \frac{1}{sL_1} \frac{\gamma_{LC}^2}{s^2 + \omega_{res}^2} \quad (1)$$

where $\omega_{res} = \sqrt{(L_1 + L_2)/(L_1 L_2 C)}$ is the natural resonant frequency. $\gamma_{LC} = \sqrt{1/(L_2 C)}$. L_1 is the inverter-side inductance. $L_2 = L_{2o} + L_s$. L_{2o} is the motor-side inductance. L_s is the motor inductance. C refers to the filtered capacitor. $i_{2s} = i_{2\alpha} + j i_{2\beta}$ is the motor current and $V_s = V_{2\alpha} + j V_{2\beta}$ denotes the inverter output voltage. The back EMF is neglected, since it only influences the fundamental motor current and has no effect on stability [11]. With zero-order hold method, the discrete-time transfer function can be obtained as

$$G_s(z) = \frac{i_{2s}(z)}{V_s(z)} = \frac{T}{(L_1 + L_2)(z - 1)} - \frac{\sin(\omega_{res}T)}{\omega_{res}(L_1 + L_2)} \frac{z - 1}{z^2 - 2z \cos(\omega_{res}T) + 1} \quad (2)$$

where T is the sampling period.

To represent the transfer function in the dq synchronous coordinate, the frequency shift $z \rightarrow z e^{j\omega_e T}$ is applied in (2), which leads to

$$G_r(z) = \frac{i_{2r}(z)}{V_r(z)} = \frac{T}{(L_1 + L_2)(z e^{j\omega_e T} - 1)} - \frac{\sin(\omega_{res}T)}{\omega_{res}(L_1 + L_2)} \frac{z e^{j\omega_e T} - 1}{z^2 e^{2j\omega_e T} - 2z e^{j\omega_e T} \cos(\omega_{res}T) + 1} \quad (3)$$

where $i_{2r} = i_{2d} + j i_{2q}$. $V_r = V_d + j V_q$. ω_e is the fundamental angular frequency. It can be checked that the resonant frequency in the synchronous coordinate varies with ω_e as

$$\omega_{res}^r = \omega_{res} - \omega_e \quad (4)$$

where ω_{res}^r denotes the synchronous resonant frequency.

Besides, the one sampling-period delay is often modeled as latched in the stationary frame [25]. Because of the synchronous transformation, the digital delay in the synchronous coordinate is modeled as

$$G_d(z) = \frac{V_r(z)}{V_r^*(z)} = \frac{1}{z e^{j\omega_e T}} \quad (5)$$

where V_r^* denotes the complex voltage reference. Therefore, the discrete-time transfer function with digital delay is derived as

$$G_p(z) = \frac{i_{2r}(z)}{V_r^*(z)} = G_r(z) \times G_d(z) \quad (6)$$

where $G_p(z)$ is the discrete-time transfer function with digital delay in the dq synchronous coordinate.

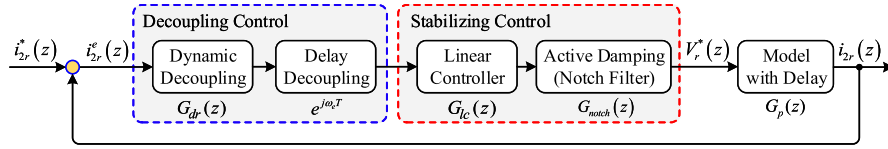


Fig. 2. System diagram of the proposed dynamic-decoupled current control.

III. PROPOSED DYNAMIC-DECOUPLED CURRENT CONTROL METHOD

In this section, a complex dynamic-decoupled current control method for the *LCL*-equipped HSPMSM is proposed, as shown in Fig. 2. The transfer function of the proposed controller is designed as

$$G_c(z) = \frac{V_r^*(z)}{i_{2r}^e(z)} = \underbrace{\frac{G_{dr}(z)}{z e^{j\omega_e T} - 1}}_{\text{Decoupling Control}} \times e^{j\omega_e T} \times \underbrace{\frac{G_{lc}(z)}{z-1} \times G_{notch}(z)}_{\text{Stabilizing Control}} \quad (7)$$

where $i_{2r}^e(z) = i_{2r}^*(z) - i_{2r}(z)$. $i_{2r}^*(z)$ is the reference current and $i_{2r}(z)$ is the regulated current error. The $G_{lc}(z)$, $G_{dr}(z)$, and $G_{notch}(z)$ denote the transfer function of the linear controller, the dynamic decoupling, and the notch filter, respectively. $e^{j\omega_e T}$ is the decoupling gain of the digital delay. a and b are coefficients of the proposed controller, which meet

$$a > 0 \quad -\frac{b}{a} \lesssim 1. \quad (8)$$

The transfer function of the discrete-time notch filter is introduced as [32]

$$G_{notch}(z) = \frac{1(1 + \lambda_2) - 2\lambda_1 z^{-1} + (1 + \lambda_2)z^{-2}}{2(1 - \lambda_1 z^{-1} + \lambda_2 z^{-2})} \quad (9)$$

and the coefficients are defined as

$$\lambda_1 = \frac{2 \cos(\omega_n T)}{1 + \tan(\Omega T/2)} \quad \lambda_2 = \frac{1 - \tan(\Omega T/2)}{1 + \tan(\Omega T/2)} \quad (10)$$

where ω_n denotes the resonant frequency of the notch filter and Ω is the -3 -dB bandwidth.

Therefore, the forward-path transfer function with the proposed controller and the discrete-time model is established as

$$\frac{i_{2r}(z)}{i_{2r}^e(z)} = G_c(z) \times G_p(z). \quad (11)$$

A. Decoupling Control

To achieve the decoupled-dynamic current control, the decoupling control is designed as follows.

1) Delay Decoupling: The item $e^{j\omega_e T}$ aims to eliminate the coupling caused by the digital delay and it provides $\omega_e T$ phase lead.

2) Dynamic Decoupling: To further decoupling, $G_{dr}(z)$ is designed to achieve the dynamic decoupling, as shown in (7). The decoupled transfer function is written as

$$G_p^d(z) = G_p(z)G_{dr}(z)e^{j\omega_e T} = \frac{T}{z(z-1)(L_1 + L_2)} - \frac{\sin(\omega_{res}T)}{z(z-1)\omega_{res}(L_1 + L_2)} \times \frac{(ze^{j\omega_e T} - 1)^2}{z^2 e^{2j\omega_e T} - 2ze^{j\omega_e T} \cos(\omega_{res}T) + 1} \quad (12)$$

where $G_p^d(z)$ represents the series transfer function with the decoupling control and the discrete-time model. Fig. 4 shows the bode diagram of $G_p^d(z)$. It can be observed that $G_p^d(z)$ at $\omega_e = 2\pi f_N$ has the same magnitude as $G_p(z)$ at $\omega_e = 0$ in the low-frequency region. It indicates the dynamic performance of $G_p^d(z)$ is decoupled in the low-frequency region. In the high-speed region, the dynamic coupling still exists. Considering the exciting component located in the high-frequency region is usually small, the dynamic-decoupled is achieved with the proposed decoupling control.

B. Stabilizing Control With AD

The stabilizing control is designed to provide sufficient PM and GM, which consists of a linear controller and a notch filter. The detailed control block of the proposed dynamic-decoupled current control method is demonstrated in Fig. 3.

C. Zero Steady-State Tracking Error

Eliminating the steady-state error is essential for a current controller. In order to discuss the steady-state performance of the proposed method, the close-loop transfer function can be derived as

$$G_{close} = \frac{i_{2r}(z)}{i_{2r}^e(z)} = \frac{G_c(z)G_p(z)}{1 + G_c(z)G_p(z)} = \frac{P(z)}{\Lambda(z) + P(z)} \quad (13)$$

and $\Lambda(z)$ and $P(z)$ are defined as

$$\Lambda(z) = z(z^2 e^{2j\omega_e T} - 2ze^{j\omega_e T} \cos(\omega_{res}T) + 1)(z-1)^2$$

$$P(z) = \left(\begin{array}{l} (\alpha_1 - \alpha_2) z^2 e^{2j\omega_e T} \\ + 2(\alpha_2 - \cos(\omega_{res}T)\alpha_1) ze^{j\omega_e T} \\ + (\alpha_1 - \alpha_2) \end{array} \right) \times (az + b) G_{notch}(z) \quad (14)$$

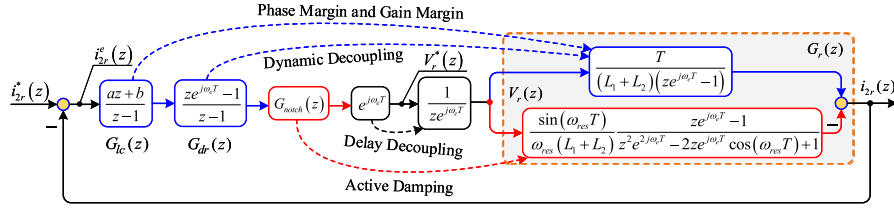


Fig. 3. Control block of the proposed dynamic-decoupled current control.

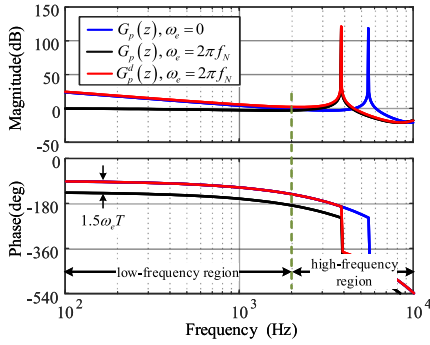


Fig. 4. Bode diagram of $G_P^d(z)$ with $f_N = 1667$ Hz and $T = 50$ μ s.

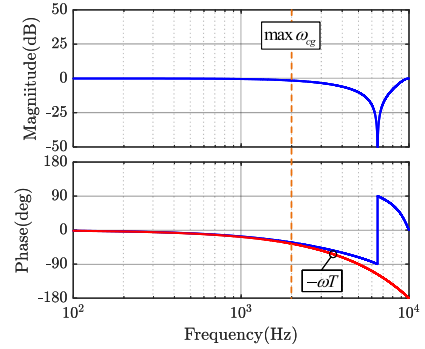


Fig. 5. Bode diagram of $G_{\text{notch}}(z)$ with $\Omega = 2\pi \times 12000$.

where α_1 and α_2 are defined as

$$\alpha_1 = \frac{T}{L_1 + L_2} \quad \alpha_2 = \frac{\sin(\omega_{\text{res}} T)}{\omega_{\text{res}} (L_1 + L_2)}. \quad (15)$$

Based on the closed-loop transfer function above, the final value of $i_{2r}(t)$ can be obtained as

$$\begin{aligned} \lim_{t \rightarrow \infty} i_{2r}(t) &= \lim_{z \rightarrow 1} (z-1) G_{\text{close}}(z) i_{2r}^*(z) \\ &= \lim_{z \rightarrow 1} (z-1) G_{\text{close}}(z) \frac{z}{z-1} \\ &= \lim_{z \rightarrow 1} z \frac{P(z)}{\Lambda(z) + P(z)} (z) i_{2r}^*. \end{aligned} \quad (16)$$

where $i_{2r}^*(z)$ is modeled as a step reference and i_{2r}^* is the amplitude of the step signal.

For $\Lambda(z)$, there is

$$\lim_{z \rightarrow 1} \Lambda(z) = 0 \quad (17)$$

and for $P(z)$, it leads to

$$\lim_{z \rightarrow 1} P(z) = \begin{pmatrix} (\alpha_1 - \alpha_2) e^{2j\omega_e T} \\ +2(\alpha_2 - \cos(\omega_{\text{res}} T)) \alpha_1 e^{j\omega_e T} \\ +(\alpha_1 - \alpha_2) \end{pmatrix} (a+b). \quad (18)$$

According to (8), $a+b \neq 0$ and, thus, the final value of $i_{2r}(t)$ can be obtained as

$$\lim_{t \rightarrow \infty} i_{2r}(t) = i_{2r}^*. \quad (19)$$

Therefore, the zero steady-state error is achieved with the proposed current controller.

IV. GAIN DETERMINATION

In this section, the coefficients of the linear controller (a and b) and the parameters (ω_n and Ω) of the notch filter are well designed to meet the requirements of the PM and GM. It should be noted that the following theoretical analysis is based on the assumption that the -180° phase crossing frequency is smaller than the synchronous resonant frequency ω_{res}^r . In that case, the LCL resonance does not affect the closed-loop stability and the coefficient selection. To ensure that, the stable region of the LCL resonance with the proposed method will be discussed in the next section.

A. Notch Filter

As the mentioned analysis, the resonant frequency ω_n should be located after the resonant frequency of the LCL filter. Considering the parameter variation, ω_n is selected with more robustness as

$$\omega_n > 1.2\omega_{\text{res}} \quad (20)$$

and Ω is selected to meet the following equation:

$$\begin{aligned} |G_{\text{notch}}(z)| (z = e^{-j\omega T}) &\approx 1 \\ \angle G_{\text{notch}}(z) (z = e^{-j\omega T}) &\approx -\omega T \end{aligned} \quad (21)$$

where ω is less than the desired -180° phase crossing frequency of the open-loop transfer function, which will be discussed later. In that case, Ω can be $2\pi \times 12000$. Clearly, Ω is unrelated with the LCL filter parameters, which means that Ω is suitable for different drive systems. Fig. 5 shows the bode diagram of $G_{\text{notch}}(z)$. It can be observed that the phase of the $G_{\text{notch}}(z)$ is almost equivalent to the $-\omega T$ before the

maximum -180° phase crossing frequency, which will be discussed later.

B. Linear Controller

Proposition 1: To achieve $PM > \pi/4$ and $GM > -3\text{dB}$, the coefficient a and b of the linear controller should be selected on basis of the following equation:

$$\begin{aligned} a &= \omega_{cp}(L_1 + L_2) \\ b &= 0.5a(\pi - 5\omega_{cg}T)\omega_{cg}T - a \\ \omega_{cp} &= t \frac{\pi}{20T} \quad \frac{2 + \sqrt{3}}{20} \frac{\pi}{T} < \omega_{cg} < \frac{\pi}{5T} \end{aligned} \quad (22)$$

where ω_{cp} is the frequency where the PM is measured, which is 0-dB gain crossing frequency. ω_{cg} is the frequency where the GM is measured, which is a -180° phase crossing frequency.

Proof: Assuming that the synchronous resonant frequency ω_{res}^r is larger than ω_{cg} , the magnitude and phase contribution of the LCL resonance is small before ω_{cg} . The plant response will always be dominated by the series inductance [5], [11]. Hence, only the low-frequency item of the plant model (12) is required, and the decoupled forward-path transfer function reduces to

$$G_p^d(z) \approx \frac{T}{z(z-1)(L_1 + L_2)} \quad (23)$$

and in that case, the magnitude and phase can be obtained as

$$\begin{aligned} |G_p^d(z)|(z = e^{-j\omega T}) &\approx \frac{1}{2 \sin(\omega T/2)} \frac{T}{L_1 + L_2} \\ \angle G_p^d(z)(z = e^{-j\omega T}) &\approx -\frac{\pi}{2} - \frac{3}{2}\omega T. \end{aligned} \quad (24)$$

For the linear controller $G_{lc}(z)$, the magnitude and phase is derived as

$$\begin{aligned} |G_{lc}(z)|(z = e^{-j\omega T}) &\approx \sqrt{a^2 + \left(\frac{a+b}{\omega T}\right)^2} \\ \angle G_{lc}(z)(z = e^{-j\omega T}) &\approx -\text{atan}\left(\frac{a+b}{\omega T a}\right). \end{aligned} \quad (25)$$

Therefore, the magnitude and phase of the forward-path transfer function can be written as

$$\begin{aligned} \left| \frac{i_{2r}(z)}{i_{2r}^e(z)} \right| (z = e^{-j\omega T}) &= \frac{T}{2(L_1 + L_2) \sin(\frac{\omega T}{2})} \sqrt{a^2 + \left(\frac{a+b}{\omega T}\right)^2} \\ \angle \frac{i_{2r}(z)}{i_{2r}^e(z)} (z = e^{-j\omega T}) &= -\frac{\pi}{2} - \frac{5}{2}\omega T - \text{atan}\left(\frac{a+b}{\omega T a}\right). \end{aligned} \quad (26)$$

To achieve a PM of the desired ψ_m at ω_{cp} , it results in

$$\left| \frac{i_{2r}(z)}{i_{2r}^e(z)} \right| (z = e^{-j\omega_{cp} T}) = 1 \quad (27)$$

$$\angle \frac{i_{2r}(z)}{i_{2r}^e(z)} (z = e^{-j\omega_{cp} T}) + \pi = \psi_m. \quad (28)$$

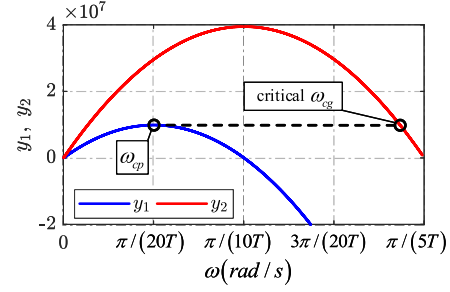


Fig. 6. Variation of y_1 and y_2 with ω .

Besides, achieve a GM of the desired δ at ω_{cg} , which leads to

$$\left| \frac{i_{2r}(z)}{i_{2r}^e(z)} \right| (z = e^{-j\omega_{cg} T}) = g \quad (29)$$

$$\angle \frac{i_{2r}(z)}{i_{2r}^e(z)} (z = e^{-j\omega_{cg} T}) + \pi = 0 \quad (30)$$

where ψ_m and δ should meet the following equation:

$$\psi_m \geq \pi/4 \quad g \leq \sqrt{2}/2. \quad (31)$$

It can be observed that it is difficult to determinate these coefficients based on (27)–(31). Therefore, according to (8), assuming that

$$\begin{aligned} \sqrt{a^2 + \left(\frac{a+b}{\omega_{cp} T}\right)^2} &\approx a \quad \sin\left(\frac{\omega T}{2}\right) = \frac{\omega T}{2} \\ \text{atan}\left(\frac{a+b}{\omega_{cp} T a}\right) &\approx \frac{a+b}{\omega_{cp} T a} \quad \text{atan}\left(\frac{a+b}{\omega_{cg} T a}\right) \approx \frac{a+b}{\omega_{cg} T a} \end{aligned} \quad (32)$$

based on (27), (29), and (31), it leads to

$$a = \omega_{cp}(L_1 + L_2) \quad (33)$$

$$t\omega_{cp} \leq 0.707\omega_{cg} \quad (34)$$

and

$$\begin{aligned} \omega_{cg} &= \frac{\pi + \sqrt{\pi^2 - 8(a+b)/a}}{10T} \\ \omega_{cp} &\leq \frac{\pi + \sqrt{\pi^2 - 160(a+b)/a}}{20T}. \end{aligned} \quad (35)$$

After math manipulation, the following equation should be satisfied with ω_{cp} and ω_{cg} :

$$-\omega_{cp}^2 + \frac{\pi}{10T}\omega_{cp} \geq -\omega_{cg}^2 + \frac{\pi}{5T}\omega_{cg}. \quad (36)$$

Defining

$$y_1 = -\omega^2 + \frac{\pi}{10T}\omega \quad y_2 = -\omega^2 + \frac{\pi}{5T}\omega \quad (37)$$

the variation of y_1 and y_2 with ω is shown in Fig. 6. To meet (36), $y_1(\omega = \omega_{cp})$ should be larger than $y_2(\omega = \omega_{cg})$. To simplify processing, the crossover frequency is selected to obtain the maximum y_1 and thus

$$\omega_{cp} = \frac{\pi}{20T}. \quad (38)$$

In that case, the critical frequency $\omega_{cg}^{\text{crit}}$ can be calculated as

$$\omega_{cg}^{\text{crit}} = \frac{2 + \sqrt{3}}{20} \frac{\pi}{T} \quad (39)$$

where $y_1(\omega = \frac{\pi}{20T})$ is equal to $y_2(\omega = \omega_{cg}^{\text{crit}})$. It can be checked that the equation $\omega_{cp} \leq 0.707\omega_{cf}^{\text{crit}}$ meets.

According to (8) and (30), the maximum ω_{cg} can be expressed as

$$\omega_{cg} = \frac{2}{5T} \left(\frac{\pi}{2} - \text{atan} \left(\frac{a+b}{\omega_{cg} T a} \right) \right) < \frac{\pi}{5T}. \quad (40)$$

Therefore, ω_{cg} should be located as

$$\frac{2 + \sqrt{3}}{20} \frac{\pi}{T} < \omega_{cg} < \frac{\pi}{5T}. \quad (41)$$

For the selection of b , on basis of (30), the coefficient b can be calculated as

$$b = 0.5a(\pi - 5\omega_{cg}T)\omega_{cg}T - a. \quad (42)$$

Based on the aforementioned analysis, when the coefficient of a and b are selected according to (33), (38), (41), and (42), both the $\text{PM} > \pi/4$ and $\text{GM} > -3\text{dB}$ are achieved. This completes the proof.

V. STABLE REGION OF THE LCL RESONANCE WITH PROPOSED METHOD

Significant research effort has been established to explore the stable region of the LCL resonance and a critical frequency (i.e., one-sixth sampling frequency) is proposed [11]. It should be noted that this conclusion is based on a stationary controller, which indicates that it is unrelated to the fundamental frequency. When taking the controller into the dq coordinate, the synchronous resonant frequency ω_{res}^r decreases with the speed up. Therefore, the stable region of the LCL resonance is limited by the maximum speed. In this section, the stable region of the LCL resonance with the proposed dynamic-decoupled current controller and coefficient selection method is discussed. A critical frequency of the LCL resonance will be given with the predefined maximum speed.

Proposition 2: With the proposed current controller (7) and coefficient selection method (22), the stable region of the LCL resonance should be

$$\omega_{\text{res}} \geq \sqrt{\frac{\rho \left(\frac{\pi}{5T} + \omega_e^m \right)^2 + \frac{1}{2} \left(\frac{\pi}{5T} + \omega_e^m \right)^4 T^2}{\rho + \frac{1}{12} \left(\frac{\pi}{5T} + \omega_e^m \right)^4 T^4}} \quad (43)$$

where ω_e^m denotes the maximum ω_e and the coefficient ρ is a positive constant, which is defined as $\rho = \frac{20\sqrt{2}\sin(0.1\pi)}{\pi} - 1$.

Proof: According to the decoupled model (12), the magnitude can be calculated as

$$\begin{aligned} |G_p^d(z)|(z = e^{-j\omega T}) &= \frac{1}{2 \sin(\frac{\omega T}{2})} \frac{T}{L_1 + L_2} \\ &\times \left(1 + \frac{\sin(\omega_{\text{res}} T)}{\omega_{\text{res}} T} \frac{(1 - \cos((\omega + \omega_e) T))^2}{\cos((\omega + \omega_e) T) - \cos(\omega_{\text{res}} T)} \right). \end{aligned} \quad (44)$$

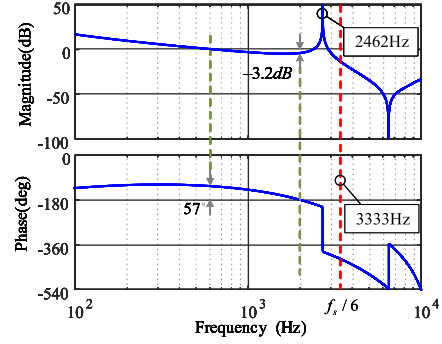


Fig. 7. Bode diagram of the open-loop transfer function when the maximum $\omega_e = 2\pi \times 1666.67$ rad/s. $\omega_{\text{res}} = 2\pi \times 4320$ rad/s. $T = 50 \mu\text{s}$.

Therefore, the magnitude of the open-loop transfer function at ω_{cg} can be written as

$$\begin{aligned} \left| \frac{i_{2r}(z)}{i_{2r}^e(z)} \right| (z = e^{-j\omega_{cg} T}) &\approx \frac{\pi}{40 \sin(\omega_{cg} T / 2)} \\ &\times \left(1 + \frac{\sin(\omega_{\text{res}} T)}{\omega_{\text{res}} T} \frac{(1 - \cos((\omega_{cg} + \omega_e) T))^2}{\cos((\omega_{cg} + \omega_e) T) - \cos(\omega_{\text{res}} T)} \right) \end{aligned} \quad (45)$$

and it leads to

$$\begin{aligned} \left| \frac{i_{2r}(z)}{i_{2r}^e(z)} \right| (z = e^{-j\omega_{cg} T}) &\approx \frac{\pi}{40 \sin(\omega_{cg} T / 2)} \\ &\times \left(1 + \left(\frac{1}{2} - \frac{(\omega_{\text{res}} T)^2}{12} \right) \frac{(\omega_{cg} + \omega_e)^4 T^2}{\omega_{\text{res}}^2 - (\omega_{cg} + \omega_e)^2} \right) \leq \frac{\sqrt{2}}{2}. \end{aligned} \quad (46)$$

Based on the coefficient selection method (22), the maximum ω_{cg} is $\frac{\pi}{5T}$. Substituting $\omega_{cg} = \frac{\pi}{5T}$ into (45), it leads to

$$\omega_{\text{res}} \geq \sqrt{\frac{\rho \left(\frac{\pi}{5T} + \omega_e \right)^2 + \frac{1}{2} \left(\frac{\pi}{5T} + \omega_e \right)^4 T^2}{\rho + \frac{1}{12} \left(\frac{\pi}{5T} + \omega_e \right)^4 T^4}}. \quad (47)$$

It can be checked that the critical ω_{res} is obtained when the maximum ω_e is adopted. This completes the proof.

When the following parameters are adopted:

$$\omega_e^m = 2\pi \times 1666 \text{ rad/s} \quad T = 50 \mu\text{s} \quad (48)$$

based on (43), the resonant frequency should be

$$\omega_{\text{res}} \geq 2\pi \times 4128 \text{ rad/s}. \quad (49)$$

Fig. 7 shows the bode diagram of the open-loop transfer function. When the critical natural resonant frequency of the LCL filter is adopted, the synchronous resonant frequency ω_{res}^r is 2462 Hz, which is smaller than the one-sixth of the sampling frequency (3333 Hz). Clearly, it results from the AD of the proposed controller. Both the PM and GM are satisfied. As a consequence, when the resonance frequency of the LCL filter does not meet (43), the effectiveness of the proposed method cannot be guaranteed.

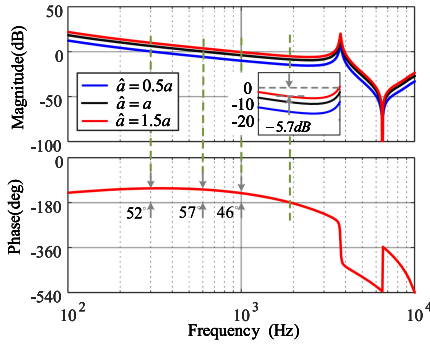


Fig. 8. Bode diagram of the open-loop transfer function when a varies. $f_N = 1666.67$ Hz and $\omega_{cg} = 2\pi \times 1950$ rad/s.

VI. ROBUSTNESS CONSIDERATIONS

In this section, the proposed controller (7) and the coefficient selection method (22) are modified with more robustness. The parameter sensitivity of the closed-loop stability is analyzed by the closed-loop pole map.

A. Robust Coefficient Selection Method

As the analysis above, the selection method of the coefficient a and b is provided, as shown in (22). a is related to the series inductance, which indicates that it will be affected by the mismatched parameters. It is equivalent with the crossover frequency ω_{cp} varying as

$$\frac{\pi}{40T} \leq \omega_{cp} \leq \frac{3\pi}{40T}. \quad (50)$$

To satisfy condition (36), ω_{cg} should be selected as

$$\frac{4 + \sqrt{13}}{40} \frac{\pi}{T} < \omega_{cg} < \frac{\pi}{5T}. \quad (51)$$

Therefore, to achieve the $PM > \pi/4$ and $GM > -3\text{dB}$ when the series inductance varies $\pm 50\%$, the coefficients of a and b should be modified as

$$\begin{aligned} a &= \omega_{cp} \hat{L}_{\text{series}} \\ b &= 0.5a (\pi - 5\omega_{cg}T) \omega_{cg}T - a \\ \omega_{cp} &= \frac{\pi}{20T} \quad \frac{4 + \sqrt{13}}{40} \frac{\pi}{T} < \omega_{cg} < \frac{\pi}{5T} \end{aligned} \quad (52)$$

where \hat{L}_{series} is the series inductance value adopted in the controller. Fig. 8 shows the bode diagram of the open-loop transfer function with the mismatched series inductance. \hat{a} is the adopted value and a is the accurate value. $f_N = 1666.67$ Hz, $T = 50\mu\text{s}$, and $\omega_{cg} = 2\pi \times 1950$ rad/s. Clearly, $PM > \pi/4$ and $GM > -3\text{dB}$ is still achieved, which indicates the coefficient selection method (52) has enhanced ability to deal with the parameter variation.

B. Modified Current Controller with More Robustness

Based on the control theory, considering the external disturbance and system noises, the pole-zero cancellation of the

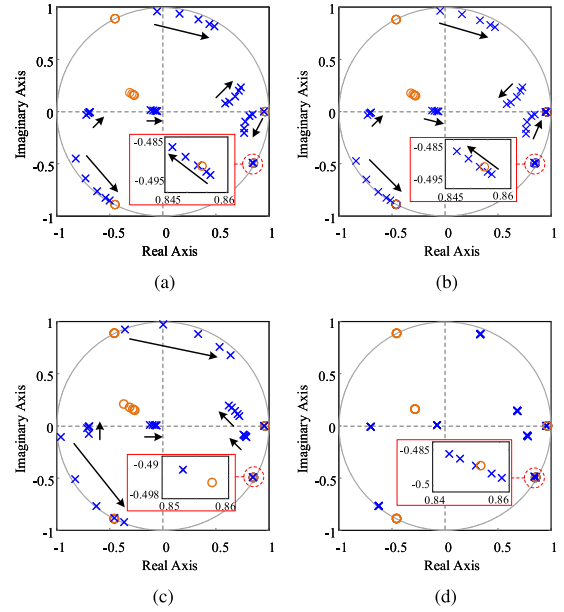


Fig. 9. Pole map of the closed-loop system with L_1 , L_2 , C , and R varying $\pm 50\%$ of their real values. $\omega_e = 2\pi f_N$. (a) $0.5L_1$ to $1.5L_1$. (b) $0.5L_2$ to $1.5L_2$. (c) $0.5C$ to $1.5C$. (d) $0.5R$ to $1.5R$.

critically stable pole may cause undesirable oscillation. It indicates that the cancellation has a lack of robustness. To solve this problem, the proposed current controller is modified by taking the motor resistance into account. With the resistance, the zero-pole cancellation will not locate at the unit cycle. Correspondingly, the robust current controller is derived as

$$\hat{G}_c(z) = \frac{V_r^*(z)}{i_{2r}^*(z)} = \frac{ze^{j\omega_e T} - \delta}{z - 1} \times e^{j\omega_e T} \times \frac{az + b}{z - 1} \times G_{\text{notch}}(z) \quad (53)$$

where $\hat{G}_c(z)$ is the modified current controller. δ is a positive coefficient and is defined as

$$\delta = e^{-\frac{R}{3L_2}T} \quad (54)$$

where R is the motor resistance. The details on the selection of δ can be found in the Appendix. Because of δ is much close to 1, the selection method of a and b , as shown in (52), is still effective for the modified current controller $\hat{G}_c(z)$.

C. Parameter Sensitivity Analysis of the Closed-Loop Stability

Fig. 9 shows the pole map of the closed-loop system with L_1 , L_2 , C , and R varying $\pm 50\%$ of their real values. In Fig. 9(a), as L_1 varies from $0.5L_1$ to $1.5L_1$, all the closed-loop poles are still inside the unit cycle, which indicates the system is stable. Besides, the variation of L_1 has slight effect on the zero-pole cancellation and, thus, the dynamic decoupling is robust against this variation. The same statement can be also applied in Fig. 9(b)–(d). Therefore, both the stability and the dynamic decoupling capability of the proposed current control method are guaranteed when L_1 , L_2 , C , and R varying $\pm 50\%$ of their real values.

TABLE I
PARAMETERS OF THE EXPERIMENTAL PLANT

Symbol	Parameter	Value
R	winding resistance	0.045Ω
L_1	inductance at the inverter side	$54\mu\text{H}$
L_{2o}	inductance at the machine side	$27.5\mu\text{H}$
L_s	inductance of the machine	$24\mu\text{H}$
C_1	capacitor of LCL filter	$31.48\mu\text{F}$
f_{res}	resonant frequency	5525Hz
U_{DC}	DC bus voltage	65V
$poles$	poles of the machine	2
f_s	switching frequency	20kHz
n_N	the rated speed	$100\text{kr}/\text{min}$

TABLE II
 q -AXIS CURRENT WITH DIFFERENT SPEED

Speed	q -axis current
38 kr/min	5A
60 kr/min	10A
80 kr/min	18A
100 kr/min	30A

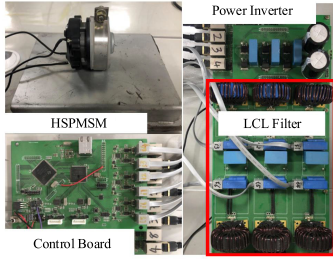


Fig. 10. Experimental setup.

VII. EXPERIMENTAL VALIDATIONS AND ANALYSIS

The experiment is designed to validate the effectiveness of the proposed method. The parameters of the experimental plant are shown in Table I. Only the current controller is used, which means no speed loop. A fan is connected to the shaft of the tested motor as a load, and thus, the load torque is approximately proportional to the square of the motor speed, as shown in Table II. The experimental setup is shown in Fig. 10. All the data of the experiments are sent to the host PC by the Ethernet module in the control board. $\delta = 0.985$, $\omega_{cg} = 2\pi \times 1950$ rad/s, $\omega_{cp} = 2\pi \times 500$ rad/s, $a = 0.3314$, and $b = -0.3235$.

A. Dynamic Decoupling Performance

Fig. 11 shows the experimental results of dynamic decoupling performance with the proposed method and conventional PI controller. $i_{2d}^* = 0$.

In Fig. 11(a), the current reference i_{2q}^* has a stepping increase from 10 to 20A at $t = 0.4\text{s}$ and, thus, the speed of the tested motor varies from 60 (1000 Hz) to 84 kr/min (1400 Hz). It can be observed that the proposed method effectively tracks i_{2q}^* with a rise time of about 2.2ms and an overshoot of about 3A. With the stepping i_{2q} , the maximum deviation of i_{2d} is 0.36A. In the high-speed region, as shown in Fig. 11(b), the current reference i_{2q}^* has a stepping change from 20 to 30A at $t = 0.35\text{s}$ and, thus,

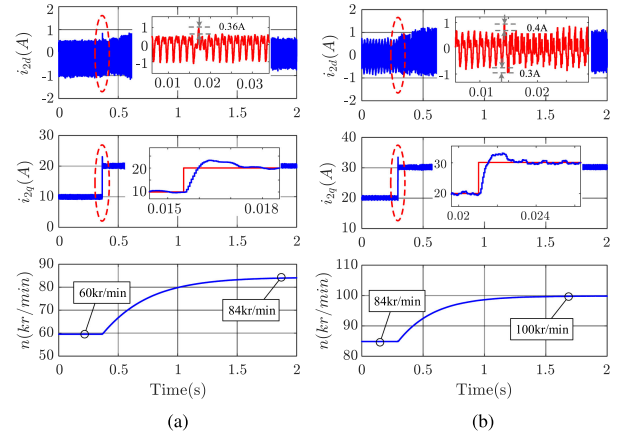


Fig. 11. Experimental results: the dynamic decoupling performance with the proposed method. From top to down: i_{2d} , i_{2q} , and speed (kr/min). (a) i_{2q} from 10 to 20 A. (b) i_{2q} from 20 to 30 A.

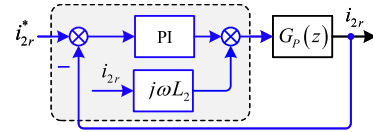


Fig. 12. Bode diagram of $G_p(z)G_{pi}(z)$.

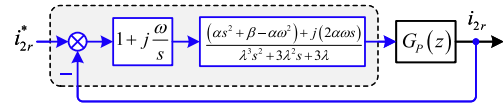


Fig. 13. Control block of the PI controller with feedforward decoupling.

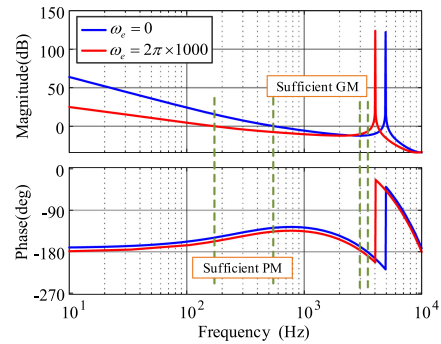


Fig. 14. Control block of the internal-mode decoupled controller [30].

the speed changes from 84 (1400 Hz) to 100 kr/min (1667 Hz). The maximum deviation of i_{2d} is 0.4A.

As a comparison with the previous methods, the current transient performance from 5 to 10A with different methods are investigated as follows.

1) Conventional PI controller, which is given as

$$G_{pi}(z) = k_p + \frac{k_i T}{z - 1} \quad (55)$$

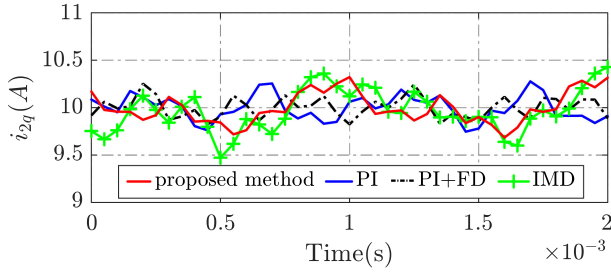


Fig. 15. Experimental results: steady-state performance comparison with previous methods at $i_{2q}^* = 10A$.

TABLE III
CONTROL PERFORMANCE COMPARISON

		PI	PI+FD	IMD	Proposed Method
Steady State	Maximum Ripple	0.62A	0.56A	1.1A	0.65A
Torque Variation 5 to 10A	Deviation of i_{2d}	3A	2.3A	1.5A	0.3A
	Overshoot of i_{2q}	1.9A	1.93A	1.85A	1.82A
	Rising time of i_{2q}	2.7ms	2.4ms	12ms	2.1ms

where $k_p = 0.4$ and $k_i = 1000$. As shown in Table II, when i_{2q} steps from 5 to 10A, the speed varies from around 38 (633 Hz) to 60 kr/min (1000 Hz). Fig. 12 shows the open-loop transfer function of the PI-controlled drive system when the motor fundamental frequency is 0 and 1000 Hz. The sufficient PM and GM are achieved with the coefficient selection.

- 2) Conventional PI controller with the feedforward decoupling (PI+FD), as shown in Fig. 13. The same coefficient selection of the PI controller is adopted.
- 3) Internal-mode decoupling (IMD) controller, as shown in Fig. 14. According to Leitner *et al.* [30], the filtering constant λ is selected as 0.00015.

Figs. 15 and 16 show the steady-state performance at 10A and the dynamic decoupling performance comparison with the previous methods from 5 to 10A, respectively. As shown in Fig. 15, the PI controller, PI+FD controller, and the proposed method have the similar steady-state performance, where the maximum current ripple is around 0.6A with the current reference 10A. But for the IMD controller, the current ripple increases up to 1.1A. In Fig. 16, with the stepping i_{2q}^* from 5 to 10A, the maximum deviation of i_{2d} is up to 3A of PI controller, 2.3A of PI+FD controller, 1.5A of IMD controller, and 0.3A of proposed method. The results of the control performance comparison with previous methods are shown in Table III.

Therefore, with the small steady-state current ripple and much reduced dynamic deviation of i_{2d} , the proposed current controller has a better steady-state performance and dynamic-decoupled ability at the same time, as the main contribution of this article.

B. Speed Control Performance With Torque Variation

Experiments are performed to evaluate the performance of the proposed controller when the speed controller is adopted and a

TABLE IV
THD ANALYSIS COMPARISON AT 30A

case 1	case 2	case 3	case 4
2.37%	2.53%	2.45%	2.23%

stepping change occurs in the load torque. In the experiment, the load torque can be changed by adjusting the air intake of the fan installed on the motor shaft.

Fig. 17 shows experimental results of the speed control performance with the proposed dynamic-decoupled current control method. In Fig. 17(a), the tested motor is driven from 0 to 80 kr/min. Besides, as shown in Fig. 17(b), at 1.55 s, the torque has a stepping change from 8 to 18A. It can be observed that the proposed current controller can well track the reference from the speed controller.

C. Robustness Validation

To validate the robustness of the proposed coefficient selection method, the following cases are considered.

- 1) Case 1: $\hat{L}_{series} = 0.5(L_1 + L_2)$, $\delta = e^{-\frac{R}{3L_2}T}$.
- 2) Case 2: $\hat{L}_{series} = 1.5(L_1 + L_2)$, $\delta = e^{-\frac{R}{3L_2}T}$.
- 3) Case 3: $\hat{L}_{series} = L_1 + L_2$, $\delta = e^{-\frac{2R}{3L_2}T}$.
- 4) Case 4: $\hat{L}_{series} = L_1 + L_2$, $\delta = e^{-\frac{R}{6L_2}T}$.

For case 1, as shown in Fig. 18(a), the current reference i_{2q}^* has a stepping increase from 20 to 30A at $t = 0.35s$. It can be observed that the proposed method still tracks i_{2q}^* effectively with a rise time of about 3.7ms and an overshoot of about 3.2A. Because of the smaller a , the rise time is much longer than that of Fig. 11(b). With the stepping i_{2q} , the maximum deviation of i_{2d} is 0.5A. In case 2, as shown in Fig. 18(b), the transient performance is achieved with a rise time of about 1.6ms and an overshoot of about 3.5A. Because of the larger a , the rise time is shorter than that of Fig. 11(b). When i_{2q} goes through changes from 20 to 30A, the maximum deviation of i_{2d} is 0.55A. According to the experimental results, the proposed current controller with the coefficient selection method works well, even when the series inductance varies $\pm 50\%$.

In case 3 and case 4, the mismatched δ is considered when $\frac{R}{L_2}$ varies from $\frac{R}{2L_2}$ to $\frac{2R}{L_2}$. In Fig. 19(a) and (b), when i_{2q} goes through changes from 20 to 30A, the maximum deviation of i_{2d} is 0.5 and 0.56A, respectively. Therefore, the dynamic decoupling performance of the proposed method is robust against the system parameters.

The THD analysis of the phase A current under different cases is also provided, as shown in Table IV. Even with parameter mismatch, the THD of the stationary current is still around 2.5%.

VIII. CONCLUSION

This article proposed a discrete-time dynamic-decoupled current control method for the LCL-equipped HSPMSM drives. The proposed current control method has the following advantages.

- 1) Robust dynamic-decoupled ability to achieve better current transient performance compared with the previous methods (PI, PI+FD, and IMD).

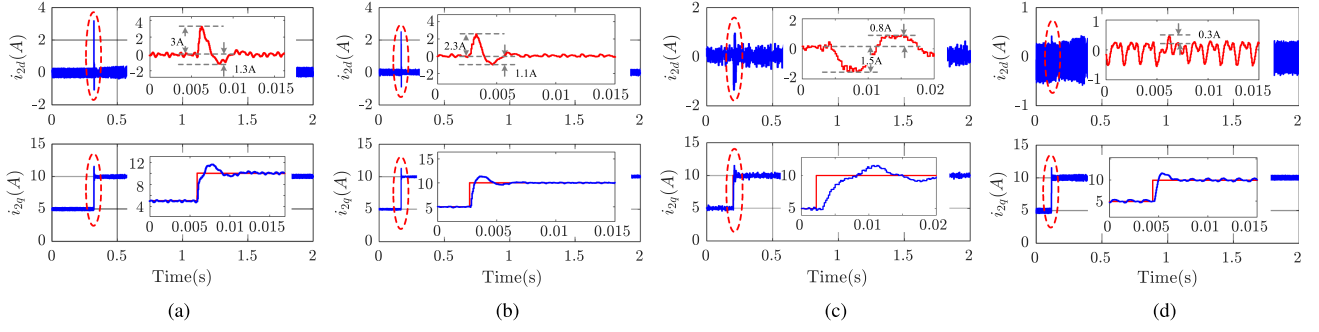


Fig. 16. Experimental results: the dynamic decoupling performance comparison with the previous methods from 5 to 10A. (a) PI controller. (b) PI+FD controller. (c) IMD controller. (d) Proposed controller.

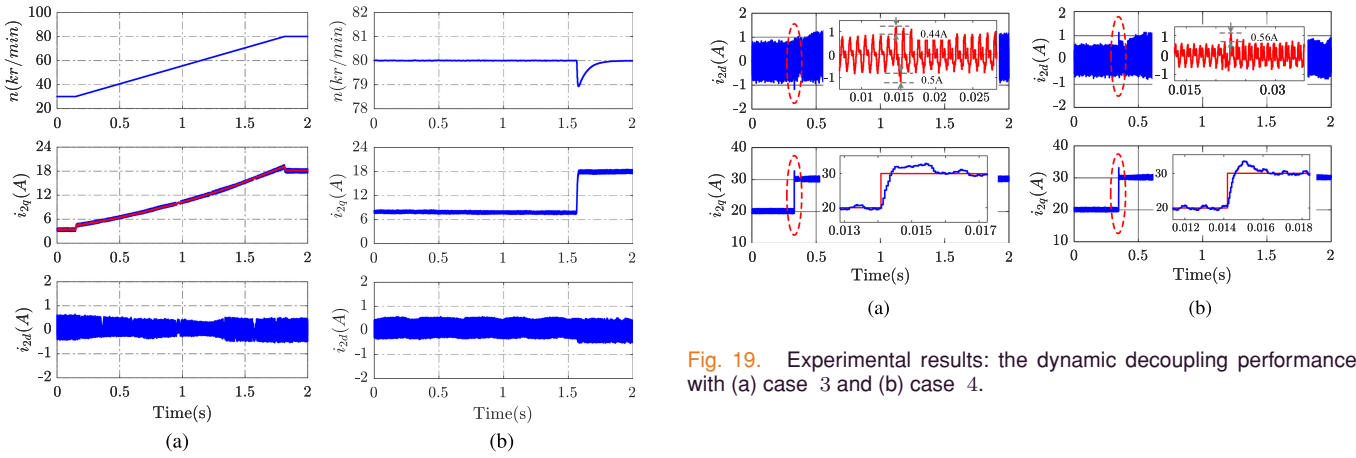


Fig. 17. Experimental result: speed control performance with torque variation at 80 kr/min. (a) Speed tracking performance. (b) Torque variation.

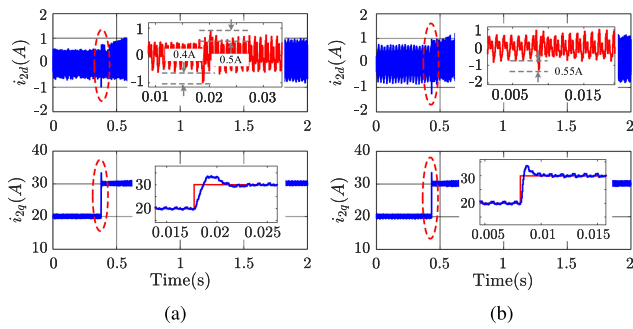


Fig. 18. Experimental results: the dynamic decoupling performance with (a) case 1 and (b) case 2.

- 2) Similar steady-state tracking performance with PI and PI+FD method, but it is much better than IMD method.
- 3) Robust coefficient selection method to achieve sufficient PM and GM, even with the system parameters varying $\pm 50\%$.

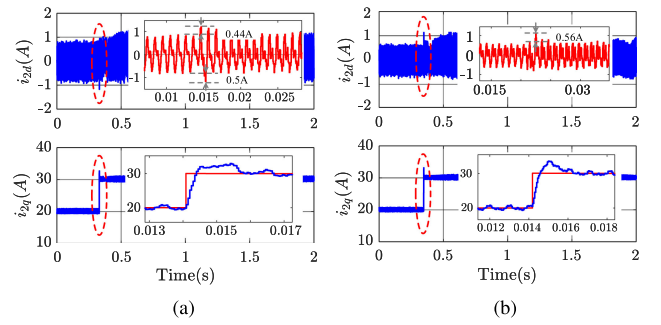


Fig. 19. Experimental results: the dynamic decoupling performance with (a) case 3 and (b) case 4.

APPENDIX

The complex continuous-time model in the $\alpha\beta$ stationary coordinate with the motor resistance is expressed as

$$G_p(s) = \frac{1}{D(s)} \quad (\text{A.1})$$

where $D(s) = \eta_1 s^3 + \eta_2 s^2 + \eta_3 s + \eta_4$ and the coefficients are defined as

$$\begin{aligned} \eta_1 &= L_1 L_2 C & \eta_2 &= L_1 C R \\ \eta_3 &= L_1 + L_2 & \eta_4 &= R. \end{aligned} \quad (\text{A.2})$$

To obtain the poles of $G_p(s)$, the discriminant Δ of the equation $D(s) = 0$ is derived as

$$\begin{aligned} \Delta &= \left(\frac{\eta_2 \eta_3}{6\eta_1^2} - \frac{\eta_2^3}{27\eta_1^3} - \frac{\eta_4}{2\eta_1} \right)^2 + \left(\frac{\eta_3}{3\eta_1} - \frac{\eta_2^2}{9\eta_1^2} \right)^3 \\ &> \left(\frac{\eta_3}{3\eta_1} - \frac{\eta_2^2}{9\eta_1^2} \right)^3 = \frac{3(L_1 + L_2) - (L_1 C R)^2}{9L_1 L_2 C} > 0. \end{aligned} \quad (\text{A.3})$$

Therefore, the equation $D(s) = 0$ has one real root and two complex conjugate roots as

$$s_1 = \sigma_1 \approx -\frac{R}{3L_2} \quad s_{2,3} = \sigma_2 \pm j\sigma_3. \quad (\text{A.4})$$

By using $z = e^{-sT}$ and the frequency shift $z \rightarrow ze^{j\omega_e T}$

$$\begin{aligned} z_1 &= e^{-\sigma_1 T} \approx e^{(-\frac{R}{3L_2} - j\omega_e)T} \\ z_{2,3} &= e^{-(\sigma_2 \pm j\sigma_3 + j\omega_e)T} \end{aligned} \quad (\text{A.5})$$

where z_1 causes the coupling of the dq coordinate and $z_{2,3}$ is the quasi-resonance poles. To achieve the zero-pole cancellation with z_1 , δ can be derived as

$$\delta = e^{-\frac{R}{3L_2} T}. \quad (\text{A.6})$$

REFERENCES

- [1] D. Gerada, A. Mebarki, N. L. Brown, C. Gerada, A. Cavagnino, and A. Boglietti, "High-speed electrical machines: Technologies, trends, and developments," *IEEE Trans. Ind. Electron.*, vol. 61, no. 6, pp. 2946–2959, Jun. 2014.
- [2] J. K. Steinke, "Use of an LC filter to achieve a motor-friendly performance of the PWM voltage source inverter," *IEEE Trans. Energy Convers.*, vol. 14, no. 3, pp. 649–654, Sep. 1999.
- [3] W. Wu, Y. Liu, Y. He, H. S. H. Chung, M. Liserre, and F. Blaabjerg, "Damping methods for resonances caused by LCL-filter-based current-controlled grid-tied power inverters: An overview," *IEEE Trans. Ind. Electron.*, vol. 64, no. 9, pp. 7402–7413, Sep. 2017.
- [4] Q. Liu, T. Caldognetto, and S. Buso, "Review and comparison of grid-tied inverter controllers in microgrids," *IEEE Trans. Power Electron.*, vol. 35, no. 7, pp. 7624–7639, Jul. 2020.
- [5] J. Wang, J. D. Yan, L. Jiang, and J. Zou, "Delay-dependent stability of single-loop controlled grid-connected inverters with LCL filters," *IEEE Trans. Power Electron.*, vol. 31, no. 1, pp. 743–757, Jan. 2016.
- [6] C. Zou, B. Liu, S. Duan, and R. Li, "Influence of delay on system stability and delay optimization of grid-connected inverters with LCL filter," *IEEE Trans. Ind. Informat.*, vol. 10, no. 3, pp. 1775–1784, Aug. 2014.
- [7] J. Yin, S. Duan, and B. Liu, "Stability analysis of grid-connected inverter with LCL filter adopting a digital single-loop controller with inherent damping characteristic," *IEEE Trans. Ind. Informat.*, vol. 9, no. 2, pp. 1104–1112, May 2013.
- [8] J. Dannehl, M. Liserre, and F. W. Fuchs, "Filter-based active damping of voltage source converters with LCL filter," *IEEE Trans. Ind. Electron.*, vol. 58, no. 8, pp. 3623–3633, Aug. 2011.
- [9] W. Yao, Y. Yang, X. Zhang, F. Blaabjerg, and P. C. Loh, "Design and analysis of robust active damping for LCL filters using digital notch filters," *IEEE Trans. Power Electron.*, vol. 32, no. 3, pp. 2360–2375, Mar. 2017.
- [10] R. A. Fantino, C. A. Busada, and J. A. Solsona, "Optimum PR control applied to LCL filters with low resonance frequency," *IEEE Trans. Power Electron.*, vol. 33, no. 1, pp. 793–801, Jan. 2018.
- [11] S. G. Parker, B. P. McGrath, and D. G. Holmes, "Regions of active damping control for LCL filters," *IEEE Trans. Ind. Appl.*, vol. 50, no. 1, pp. 424–432, Jan. 2014.
- [12] M. Ben Saïd-Romdhane, M. W. Naouar, I. Slama-Belkhdja, and E. Monmasson, "Robust active damping methods for LCL filter-based grid-connected converters," *IEEE Trans. Power Electron.*, vol. 32, no. 9, pp. 6739–6750, Sep. 2017.
- [13] E. Rodriguez-Diaz, F. D. Freijedo, J. C. Vasquez, and J. M. Guerrero, "Analysis and comparison of notch filter and capacitor voltage feedforward active damping techniques for LCL grid-connected converters," *IEEE Trans. Power Electron.*, vol. 34, no. 4, pp. 3958–3972, Apr. 2019.
- [14] D. Pan, X. Ruan, C. Bao, W. Li, and X. Wang, "Optimized controller design for LCL-type grid-connected inverter to achieve high robustness against grid-impedance variation," *IEEE Trans. Ind. Electron.*, vol. 62, no. 3, pp. 1537–1547, Mar. 2015.
- [15] Y. He, X. Wang, X. Ruan, D. Pan, and K. Qin, "Hybrid active damping combining capacitor current feedback and point of common coupling voltage feedforward for LCL-type grid-connected inverter," *IEEE Trans. Power Electron.*, vol. 36, no. 2, pp. 2373–2383, Feb. 2021.
- [16] Y. He, X. Wang, X. Ruan, D. Pan, X. Xu, and F. Liu, "Capacitor-current proportional-integral positive feedback active damping for LCL-type grid-connected inverter to achieve high robustness against grid impedance variation," *IEEE Trans. Power Electron.*, vol. 34, no. 12, pp. 12423–12436, Dec. 2019.
- [17] J. Kukkola, M. Hinkkanen, and K. Zenger, "Observer-based state-space current controller for a grid converter equipped with an LCL filter: Analytical method for direct discrete-time design," *IEEE Trans. Ind. Appl.*, vol. 51, no. 5, pp. 4079–4090, Sep. 2015.
- [18] E. Wu and P. W. Lehn, "Digital current control of a voltage source converter with active damping of LCL resonance," *IEEE Trans. Power Electron.*, vol. 21, no. 5, pp. 1364–1373, Sep. 2006.
- [19] C. A. Busada, S. G. Jorge, and J. A. Solsona, "Full-state feedback equivalent controller for active damping in LCL-filtered grid-connected inverters using a reduced number of sensors," *IEEE Trans. Ind. Electron.*, vol. 62, no. 10, pp. 5993–6002, Oct. 2015.
- [20] R. A. Fantino, C. A. Busada, and J. A. Solsona, "Observer-based grid-voltage sensorless synchronization and control of a VSI-LCL tied to an unbalanced grid," *IEEE Trans. Ind. Electron.*, vol. 66, no. 7, pp. 4972–4981, Jul. 2019.
- [21] Y. Guan, Y. Wang, Y. Xie, Y. Liang, A. Lin, and X. Wang, "The dual-current control of grid-connected inverter with LCL filter," *IEEE Trans. Power Electron.*, vol. 34, no. 6, pp. 5940–5952, Jun. 2019.
- [22] Y. Wang and R.-J. Wai, "Design of discrete-time backstepping sliding-mode control for LCL-type grid-connected inverter," *IEEE Access*, vol. 8, pp. 95082–95098, 2020.
- [23] J. R. Massing, M. Stefanello, H. A. Grundling, and H. Pinheiro, "Adaptive current control for grid-connected converters with LCL filter," *IEEE Trans. Ind. Electron.*, vol. 59, no. 12, pp. 4681–4693, Dec. 2012.
- [24] J. Dannehl, F. W. Fuchs, and P. B. Thøgersen, "PI state space current control of grid-connected PWM converters with LCL filters," *IEEE Trans. Power Electron.*, vol. 25, no. 9, pp. 2320–2330, Sep. 2010.
- [25] H. Kim, M. W. Degner, J. M. Guerrero, F. Briz, and R. D. Lorenz, "Discrete-time current regulator design for AC machine drives," *IEEE Trans. Ind. Appl.*, vol. 46, no. 4, pp. 1425–1435, Jul. 2010.
- [26] C. A. Busada, S. G. Jorge, and J. A. Solsona, "A synchronous reference frame PI current controller with dead beat response," *IEEE Trans. Power Electron.*, vol. 35, no. 3, pp. 3097–3105, Mar. 2020.
- [27] Y. Wang, C. Wang, W. Zeng, and F. Bai, "Multifactorial prediction errors analysis and a feedback self-correction on model predictive control for the three-phase inverter," *IEEE Trans. Ind. Electron.*, vol. 66, no. 5, pp. 3647–3654, May 2019.
- [28] X. Zhang, L. Zhang, and Y. Zhang, "Model predictive current control for PMSM drives with parameter robustness improvement," *IEEE Trans. Power Electron.*, vol. 34, no. 2, pp. 1645–1657, Feb. 2019.
- [29] M. Wang, X. Wang, J. Qiao, and L. Wang, "Improved current decoupling method for robustness improvement of LCL-type STATCOM based on active disturbance rejection control," *IEEE Access*, vol. 7, pp. 121781–121792, 2019.
- [30] S. Leitner, M. Yazdani, S. Ziaeinejad, A. Mehrizi-Sani, and A. Muetze, "Internal model-based active resonance damping current control of a grid-connected voltage-sourced converter with an LCL filter," *IEEE Trans. Power Syst.*, vol. 33, no. 6, pp. 6025–6036, Nov. 2018.
- [31] M. Su *et al.*, "Single-sensor control of LCL-filtered grid-connected inverters," *IEEE Access*, vol. 7, pp. 38481–38494, 2019.
- [32] K. Hirano, S. Nishimura, and S. Mitra, "Design of digital notch filters," *IEEE Trans. Circuits Syst.*, vol. 21, no. 4, pp. 540–546, Jul. 1974.



the high-speed drive system with LCL output filter.

Yu Yao (Student Member, IEEE) received the B.S. degree in electrical engineering in 2016 from Southeast University, Nanjing, China, where he is currently working toward the Doctor of Engineering degree in electric machines and control with the School of Electrical Engineering.

His main research interests include the design of the power inverter, current regulator design, position sensorless drive for the high-speed PMSM, and active damping methods for



Yunkai Huang received the M.Sc. and Ph.D. degrees in electrical engineering from Southeast University, Nanjing, China, in 2001 and 2007, respectively.

He is currently a Professor with the School of Electrical Engineering, Southeast University. His research interests include design and control of PM machine and high-speed machine, applications in domestic appliances, electric vehicles, railway traction, all-electric ships, more-electric aircraft, and wind power generation

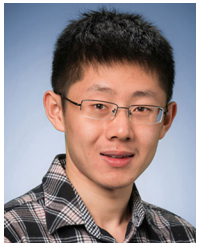
systems.



Jianning Dong (Member, IEEE) received the B.S. and Ph.D. degrees in electrical engineering from Southeast University, Nanjing, China, in 2010 and 2015, respectively.

He has been an Assistant Professor with the Delft University of Technology, Delft, The Netherlands, since 2016. Before joining TU Delft, he was a Postdoc Researcher with McMaster Automotive Resource Centre, McMaster University, Hamilton, ON, Canada. His main research interests include design, modeling, and

control of electromechanical systems.



Fei Peng (Member, IEEE) received the B.S. and M.S. degrees in electrical engineering from Southeast University, Nanjing, China, in 2010 and 2012, respectively, and the Ph.D. degree in electrical and computer engineering from McMaster University, Hamilton, ON, Canada, in 2016.

He was a Postdoctoral Fellow with the McMaster Institute for Automotive Research and Technology, McMaster University. In December 2016, he joined the School of Electrical Engineering, Southeast University, as an Assistant Professor. His research interests include optimal design and control of power converters, modeling, and digital control of motor drives.

engineering, Southeast University, as an Assistant Professor. His research interests include optimal design and control of power converters, modeling, and digital control of motor drives.



Zichong Zhu (Student Member, IEEE) received the B.S. degree in thermal energy and power engineering from the Nanjing Institute of Technology, Nanjing, China, in 2014, and the Ph.D. degree in electrical engineering from Southeast University, Nanjing, in 2021.

He joined Nanjing Tech University, Nanjing, as a Lecturer in 2021. His research interests include electromagnetic analysis, thermal management, and structural design of the permanent magnet synchronous machines for the

wheel-hub driving, turbo and servo applications.